MARCH 10 2026

Reconstructing the vibroacoustic response of thin isotropic plates under distorted similitude: A wavenumber-based approach

Alessandro Casaburo

J. Acoust. Soc. Am. 159, 2085–2095 (2026)
https://doi.org/10.1121/10.0042990

JASA ARTICLE

Reconstructing the vibroacoustic response of thin isotropic plates under distorted similitude: A wavenumber-based approach

Alessandro Casaburo[a)]
Pasta-Lab, Industrial Engineering Department, University of Naples Federico II, Via Claudio 21, Naples 80125, Italy

ABSTRACT:
Similitude methods are widely used across engineering fields to reduce cost and setup complexity in experimental testing. Several approaches have been proposed in the literature, all relying on specified similitude conditions whose satisfaction is necessary to accurately reconstruct the vibroacoustic response of a structure. When these conditions are violated, the reconstruction fails because the order and spacing of resonance modes differ from those of the reference prototype, producing a distorted similitude. To address this, a wavenumber-based method is proposed, assigning mode-dependent scale factors to natural frequencies and to the vibroacoustic response, expressed in terms of the modal wavevector components. The key idea is that wavenumber information enables direct identification and reconstruction of the prototype's resonance mode shapes, independent of their ordering. Numerical and experimental validations on thin isotropic plates show accurate reconstructions of natural frequencies, mobility, and radiated acoustic-power peaks, paving the way for applications to more complex structural configurations.
 https://doi.org/10.1121/10.0042990

(Received 9 December 2025; revised 14 February 2026; accepted 19 February 2026; published online 10 March 2026)

[Editor: Laurent Maxit] Pages: 2085–2095

I. INTRODUCTION

Experimental testing is often the final and most important validation step in many engineering fields. However, full-scale tests are frequently expensive, time consuming, and complex to set up (Casaburo *et al.*, 2019). A widely adopted alternative is to rely on similitude theory and its associated methods.

Similitude methods provide the tools to design a scaled (down or up) model, on which experiments can be conducted more efficiently, and the scaling laws needed to reconstruct the full-scale prototype response from the model measurements.

Several similitude methods have been proposed in the literature. The most widely used is dimensional analysis, based on Buckingham's Π theorem; an early application to structural problems is due to Goodier and Thomson (1944), where dimensionless invariants link systems in similitude. A second family comprises scaling with governing equations through the similitude theory applied to governing equations (STAGE) method, which applies scale factors directly to the field equations. Within this line, Simitses and co-authors contributed extensively to laminated structures under various loads and configurations, including bending, buckling, and free vibration of laminated plates (Simitses and Rezaeepazhand, 1993), as well as the flutter of symmetric (Rezaeepazhand and Yazdi, 2011) and antisymmetric (Yazdi and Rezaeepazhand, 2011) cross-ply laminated plates.

A different direction is given by energy-based approaches. Kasivitamnuay and Singhatanadgid (2005) derived scaling laws from energy conservation. Subsequently, De Rosa and Franco (2008) introduced asymptotical scaled modal analysis to reduce the spatial extent of models and save computational cost in finite-element analysis. This was later generalized into SAMSARA (similitude and asymptotic models for structural-acoustic research applications), a flexible framework used for aluminum (Meruane *et al.*, 2016) and sandwich plates (Casaburo *et al.*, 2021). Similitude laws under fluid loading were derived for isotropic, composite, and stiffened plates subjected to turbulent boundary-layer excitation (Franco *et al.*, 2019; Franco *et al.*, 2020). The near- and far-field acoustic radiation of orthotropic plates within a similitude framework was investigated by Berry *et al.* (2020), whereas Plouseau-Guédé *et al.* (2025) examined the vibroacoustic response of structures under heavy-fluid loading, a regime in which structural and acoustic responses are strongly coupled.

Sensitivity-based methods have also been explored. Luo *et al.* (2016) proposed principles to derive similitude conditions from sensitivity considerations, while Adams *et al.* (2018) formulated sensitivity-based scaling laws, in contrast to traditional similitude-based laws.

More recent work has proposed alternative routes, including finite similitude for anisotropic scaling (Davey *et al.*, 2020) and transformation matrix approaches such as VOODOO (versatile offset operator for the discrete

[a)]Email: alessandro.casaburo@unina.it

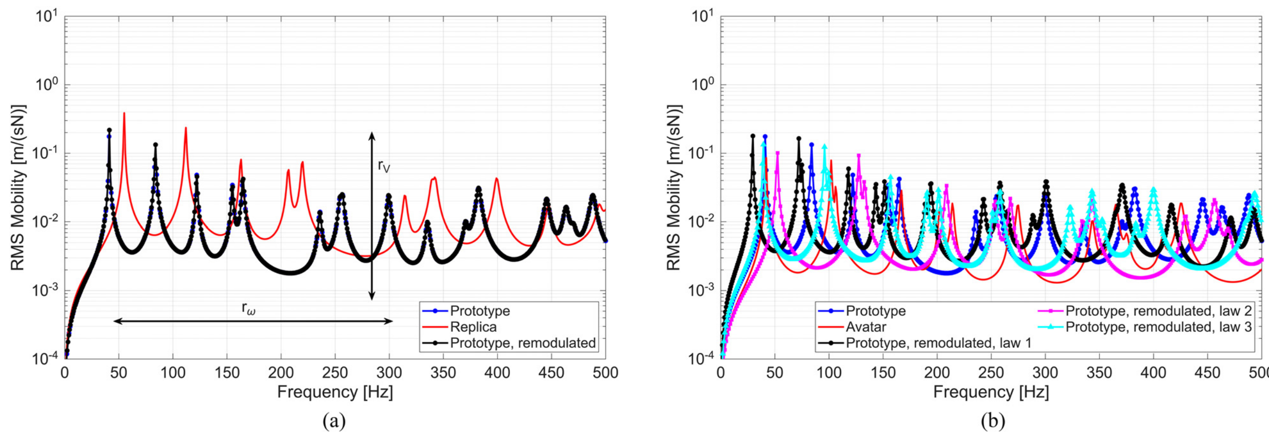

FIG. 1. RMS, spatially averaged mobility of a plate in similitude. Remodulation from a replica (a) and from an avatar (b).

observation of objects) by De Rosa *et al.* (2021). For an overview of methods, structural classes, and application domains in similitude theory, the interested reader can refer to Casaburo *et al.* (2019).

Many similitude methods can be summarized as follows:

1. Define scale factors for the relevant physical quantities, $r_X = X_p/X_m$, where subscripts p and m denote prototype and model, respectively.
2. Derive the set of similitude conditions (this step is method-dependent).
3. From these conditions, establish the scaling laws for the target variables (e.g., natural frequencies and frequency response for dynamics; deflection or absorbed energy for impact; yield stress for constitutive behavior, etc.).

If the similitude conditions are satisfied, the scaling laws are unique and provide a complete, accurate reconstruction of the outputs. In structural dynamics, the main variables of interest are the natural frequencies, the frequency response function (FRF), and vibroacoustic metrics such as radiated acoustic power. In this case, the similitude is *complete*, and the model is termed a *replica*. Conversely, if even one condition is violated, multiple, non-unique scaling laws result and none will reliably reconstruct either the natural frequencies or the FRF. The similitude is then *distorted*, and the model is termed an *avatar*.

A distorted similitude is not merely an analytical inconvenience: practical testing constraints often necessitate avatars. Manufacturing limits and facility size (e.g., wind tunnel or test cabin dimensions) can preclude the use of a replica.

Several approaches are formulated under the assumption that similitude conditions are satisfied; therefore, violations of these conditions typically lead to inaccurate reconstruction. For example, STAGE, SAMSARA, and sensitivity-based frameworks typically derive identical similitude conditions for a given class of structures and, therefore, exhibit the same reconstruction limitations when those conditions are violated. Other approaches (e.g., VOODOO) do not explicitly enforce similitude conditions; however, they still do not to recover the dynamic response when structural modifications effectively correspond to violations of those conditions. This brief literature review thus suggests that dedicated distorted similitude procedures for vibroacoustic metrics are still limited in the literature, in both vibrational (Adams *et al.*, 2018; Meruane *et al.*, 2016; Simitses and Rezaeepazhand, 1993) and acoustic contexts (Berry *et al.*, 2020; Plouseau-Guédé *et al.*, 2025).

Figure 1 illustrates the source of these difficulties. The plots report the reconstruction of the spatially averaged root mean square (RMS) mobility over 0–500 Hz for an aluminum simply supported plate of size $0.658 \times 0.478 \times 0.0025\ \mathrm{m}^3$, using similitude conditions and scaling laws derived with the SAMSARA method (Meruane *et al.*, 2016). In this approach, similitude

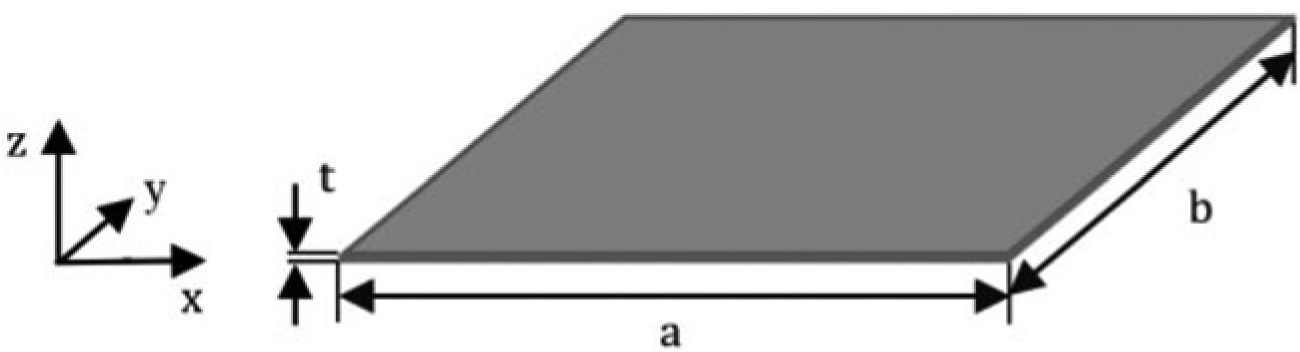

FIG. 2. Geometry of the plate.

https://doi.org/10.1121/10.0042990

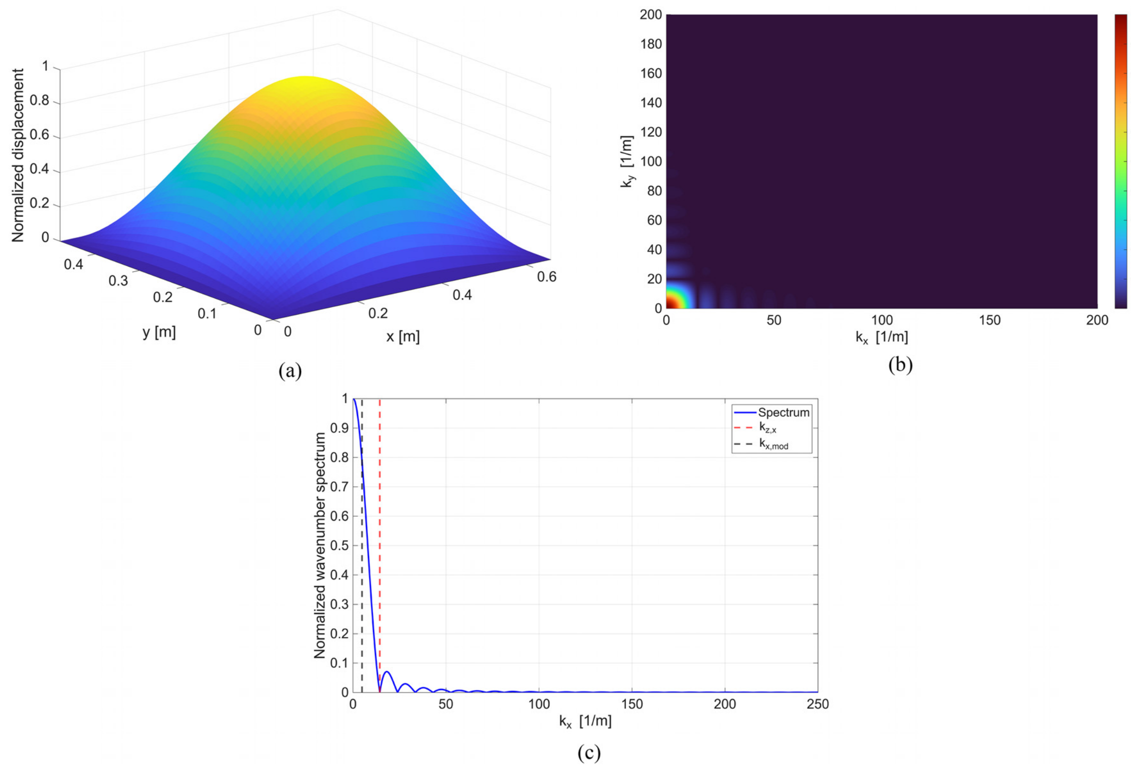

FIG. 3. Steps of the wavenumber-based approach: (a) modal analysis and mode shape, (b) normalized spectrum in wavenumber space, (c) determination of the modal wavevector components.

requires the plate length a and width b to scale equally, i.e., $r_a = r_b$. When this condition is satisfied and the material properties are unchanged, the natural frequencies scale as $r_\omega = r_t/r_a^2$ (or, equivalently, $r_\omega = r_t/r_b^2$), where r_t denotes the thickness scale factor. In Fig. 1(a), a replica with $r_a = r_b = r_t = 0.75$ is considered: a single, invariant frequency scale factor r_ω correctly aligns the resonance peaks, while a unique velocity scale factor r_V provides the proper amplitude modulation; the reconstruction is accurate across the band. Conversely, Fig. 1(b) shows an avatar characterized by $r_a = 0.94$ and $r_b = r_t = 1.25$. The violation of the similitude condition leads to multiple possible laws for the frequency scale factor, namely, r_t/r_a^2, r_t/r_b^2, and $r_t/r_a r_b$ [labelled as law 1, law 2, and law 3 in Fig. 1(b), respectively]. Despite the availability of several scaling laws, the response is not accurately reconstructed because the modal sequence and spacings differ from those of the prototype.

Distortions alter the modal basis of structures: the modal sequence and modal frequency separation change. Replicas preserve this ordering, so invariant scale factors, as implicitly assumed by many methods, can remap frequencies, aligning the natural frequencies, and scale amplitudes. For avatars, instead, those invariants no longer apply because the modal basis has been modified.

Motivated by this, a wavenumber-based reconstruction for distorted similitude is proposed and validated on thin isotropic plates under distorted similitude. The method assigns mode-dependent scale factors to natural frequencies and to the dynamic response by first estimating, for each mode, the modal-wavenumber scale factor extracted at resonance from the mode shapes via spatial-wavenumber transforms. In this way, the reconstruction directly targets the corresponding resonances, independent of their order in frequency, circumventing mode reordering. The resulting scaling laws follow from general relations (e.g., the dispersion relation), rather than from boundary condition-dependent analytical formulations, such as those governing natural frequencies. Moreover, the approach does not require explicit similitude conditions, reducing the complexity and limitations of prior frameworks. From the operating point of view, only the prototype's geometric and material information is required: the dynamic response is completely predicted.

The remainder of the paper is organized as follows. Section II derives the scaling laws employed herein. Section III presents the proposed method step by step. Section IV reports the numerical validation on two avatars under two boundary conditions, and Sec. V presents the experimental validation. Conclusions and directions for future work are given in Section VI.

II. DERIVATION OF THE SCALING LAWS

The plate geometry adopted in this work is shown in Fig. 2. The plate is assumed to be thin, isotropic, and homogeneous, governed by the Kirchhoff–Love theory.

The first scaling law concerns the natural frequencies, which is fundamental for scaling the FRF. Frequency ω and wavenumber k are linked by the phase velocity c through

TABLE I. Geometric and scaling properties of prototype and avatars.

	Prototype	Avatar, small distortion	Avatar, large distortion
a [m]	0.658	0.617	0.585
b [m]	0.478	0.382	0.273
t [m]	0.0025	0.0020	0.0020
r_a	—	1.07	1.13
r_b	—	1.25	1.75
r_t	—	1.25	1.25
r_a/r_b	—	0.85	0.64

TABLE II. Properties of aluminum 6061 alloy.

Young's modulus [Pa]	Mass density [kg/m^3]	Poisson's ratio
71×10^9	2700	0.33

the dispersion relation (Cremer *et al.*, 2005). For the prototype,

$$\omega_p = c_p k_p, \tag{1}$$

and, introducing the scale factors r_ω, r_c, and r_k,

$$\omega_p = r_\omega \omega_m = r_c c_m r_k k_m, \tag{2}$$

hence

$$r_\omega = r_c r_k. \tag{3}$$

For flexural waves in thin isotropic plates, the phase velocity of the prototype is (Cremer *et al.*, 2005)

$$c_p = \left(\frac{D_p}{\rho_p t_p}\right)^{1/4} \omega_p^{1/2}, \tag{4}$$

where D_p is the bending stiffness, ρ_p the mass density, and t_p the thickness. Rewriting Eq. (4) in terms of model quantities and the scale factors r_D, r_ρ, and r_t gives

$$c_p = r_c c_m = \left(\frac{r_D D_m}{r_\rho \rho_m r_t t_m}\right)^{1/4} (r_\omega \omega_m)^{1/2}, \tag{5}$$

from which the velocity scaling law follows

$$r_c = \left(\frac{r_D}{r_\rho r_t}\right)^{1/4} r_\omega^{1/2}. \tag{6}$$

Combining Eqs. (3) and (6) yields the frequency scaling law

$$r_{\omega(m,n)} = \sqrt{\frac{r_D}{r_\rho r_t}} r^2_{k(m,n)}, \tag{7}$$

where the indices (m, n) emphasize mode dependence under distorted similitude.

Usually, r_D, r_ρ, and r_t are known from the prototype's geometry and materials, whereas $r_{k(m,n)}$ must be estimated from modal wavenumbers. While the model's modal wavenumbers are available from experiments or numerical simulations, typical operating conditions of similitude methods assume that only the prototype's geometry and material properties are known, with no information about its frequency response, i.e., its modal wavenumbers. This issue can be bypassed by noting that, for rectangular thin, isotropic, and homogeneous plates governed by the Kirchhoff–Love theory, the modal wavenumber components can be expressed as a boundary condition- and mode-dependent dimensionless coefficient divided by the corresponding plate dimension (Hambric and Barnard, 2018; Leissa, 1969). When prototype and model share the same boundary conditions, these dimensionless coefficients cancel out in the scale factor for the same mode shape. As a result, the wavevector components along the sides of the plate (assumed parallel to the x and y axes) scale as $k_x \propto 1/a$ and $k_y \propto 1/b$. The scale factor of the x-component of the wavenumber is, therefore, given by

$$r_{k_x} = \frac{k_{x,p}}{k_{x,m}} = \frac{a_m}{a_p} = \frac{1}{r_a}. \tag{8}$$

Consequently, the x component of the wavevector of the prototype can be estimated as

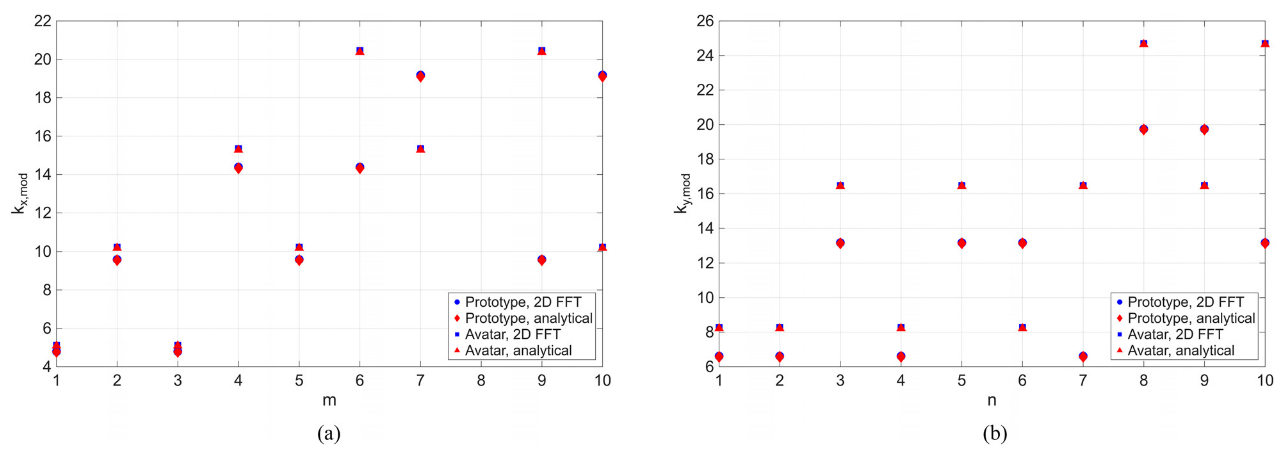

FIG. 4. Prototype and avatar modal wavevector components along x and y estimated with Eq. (18) and 2D FFT.

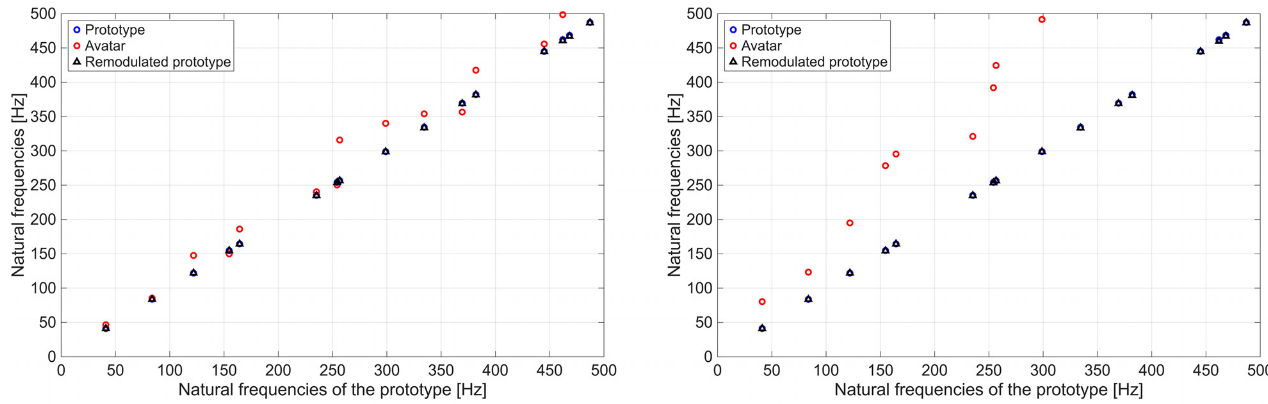

(a) (b)

FIG. 5. Reconstruction of prototype natural frequencies from the avatar. Simply supported boundary conditions, small (a) and large (b) distortion.

$$k_{x,p} = \frac{k_{x,m}}{r_a}, \tag{9}$$

and the y component can be calculated in a similar way through the width scale factor, r_b, namely,

$$k_{y,p} = \frac{k_{y,m}}{r_b}. \tag{10}$$

After this, it is straightforward to calculate the magnitude of the wavevector of the prototype and avatar with (Sheperd and Hambric, 2012)

$$|\tilde{\mathbf{k}}| = \sqrt{k_x^2 + k_y^2}, \tag{11}$$

and the corresponding scale factor to introduce in Eq. (7).

The mobility FRF is considered. The amplitude scale factor r_V is taken from the SAMSARA framework (Meruane *et al.*, 2016)

$$r_{V(m,n)} = \frac{1}{r_M r_{\omega(m,n)}}, \tag{12}$$

where r_M is the mass scale factor. The amplitude scale factor is mode dependent, too.

To illustrate that the approach extends to other vibroacoustic metrics, the radiated acoustic power of the plate is also reconstructed with the same logic, using the matrix formulation (Elliott and Johnson, 1993). If the prototype domain is discretized into N_x and N_y points along the x and y directions, respectively, the radiated power evaluated over the resulting uniform grid of $N_x \times N_y = N_G$ points is given by

$$\Pi_{rad,p}(\omega_p) = \frac{\omega_p^2 \rho_0}{4\pi c_0} \{V_p(\omega_p)\}^H [A_p][R_p(\omega_p)][A_p]\{V_p(\omega_p)\}, \tag{13}$$

where ρ_0 and c_0 are the fluid density and sound speed, $\{V_p(\omega_p)\} \in \mathbb{C}^{N_G}$ is the mobility response vector of the prototype, and $[A_p]$ is the diagonal matrix of equivalent patch areas,

$$A_p = \begin{bmatrix} A_1 & 0 & \cdots & 0 \\ 0 & A_2 & \cdots & 0 \\ \vdots & \vdots & \ddots & \vdots \\ 0 & 0 & \cdots & A_{N_G} \end{bmatrix}, \tag{14}$$

$$A_i = \frac{ab}{(N_x - 1)(N_y - 1)},$$

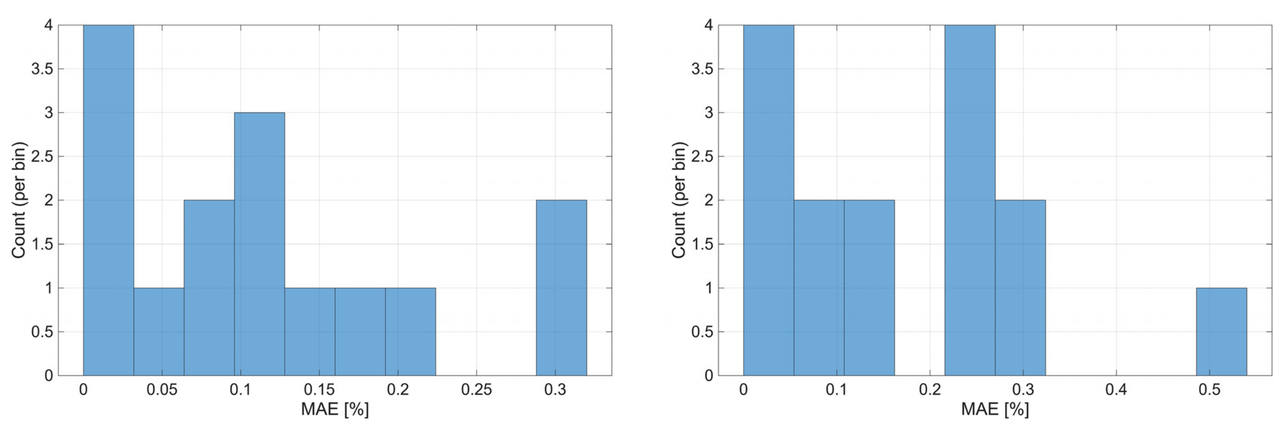

(a) (b)

FIG. 6. Distribution of the percentage MAE. Simply supported boundary condition, small (a) and large (b) distortion.

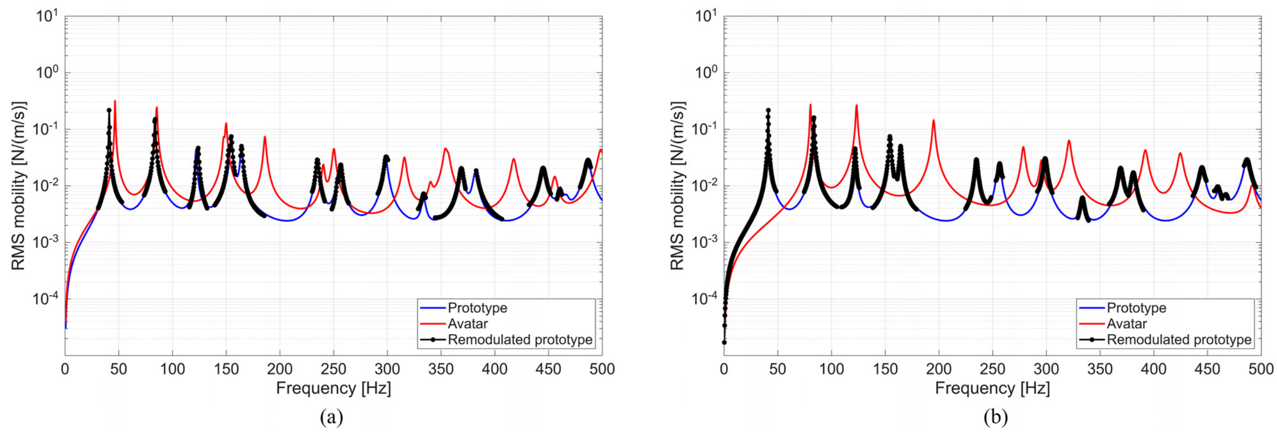

FIG. 7. Reconstruction of the spatially averaged RMS mobility. Simply supported boundary condition, small (a) and large (b) distortion.

with a and b the plate length and width. The radiation resistance matrix $[R_p(\omega_p)] \in \mathbb{R}^{N_G \times N_G}$ is a collection of sinc functions taking into account the distance between pairwise grid points,

$$R_p(\omega_p) = \begin{bmatrix} 1 & \dfrac{\sin(k_0 d_{1,2})}{k_0 d_{1,2}} & \cdots & \dfrac{\sin(k_0 d_{1,N_G})}{k_0 d_{1,N_G}} \\ \dfrac{\sin(k_0 d_{2,1})}{k_0 d_{1,2}} & 1 & \cdots & \dfrac{\sin(k_0 d_{2,N_G})}{k_0 d_{1,2}} \\ \vdots & \vdots & \ddots & \vdots \\ \dfrac{\sin(k_0 d_{N_G,1})}{k_0 d_{N_G,1}} & \dfrac{\sin(k_0 d_{N_G,2})}{k_0 d_{N_G,2}} & \cdots & 1 \end{bmatrix}, \quad (15)$$

where $k_0 = \omega/c_0$ is the acoustic wavenumber, and $d_{i,j}$ is the distance between the jth and ith grid points.

The N_G grid points in Eq. (15) are defined as the centers of radiating patches with area A_i. In practice, the velocity at the patch center can be approximated by the values measured at the patch corners (i.e., the numerical/experimental mesh nodes), provided that the characteristic dimension of the elementary radiator is small compared to the relevant wavelengths. In particular, the element size must be smaller than both the acoustic and structural wavelengths (λ_{str} and λ_{ac}, respectively).

Because the entries of $[R_p(\omega_p)]$ depend on the pairwise distances $d_{i,j}$, they do not admit a single global scale factor under general geometric distortions; consequently, no closed-form, one-factor law analogous to Eqs. (7)–(12) exists for the radiated acoustic power. This is not a limitation for reconstruction: the prototype power can be assembled by evaluating the prototype radiation matrix and inserting the scaled model quantities,

$$\Pi_{rad,p}(r_\omega \omega_m) = \frac{r_\omega^2 \omega_m^2 \rho_0}{4\pi c_0} \left\{ r_V V_m(r_\omega \omega_m) \right\}^H [r_A A_m] \times [R_p(r_\omega \omega_m)][r_A A_m] \left\{ r_V V_m(r_\omega \omega_m) \right\}, \quad (16)$$

where the mode-dependent frequency and velocity scale factors are used (subscripts omitted for compactness), and r_A is the equivalent area scale factor. The radiation resistance matrix is formulated directly in prototype coordinates and remodulated only in frequency. Its entries

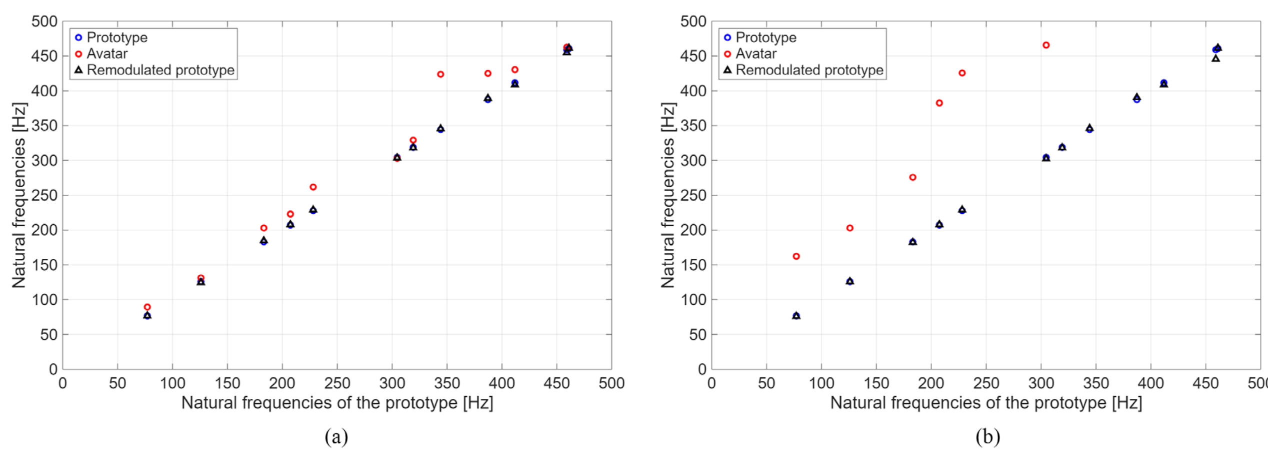

FIG. 8. Reconstruction of prototype natural frequencies from the avatar. Clamped boundary conditions, small (a) and large (b) distortion.

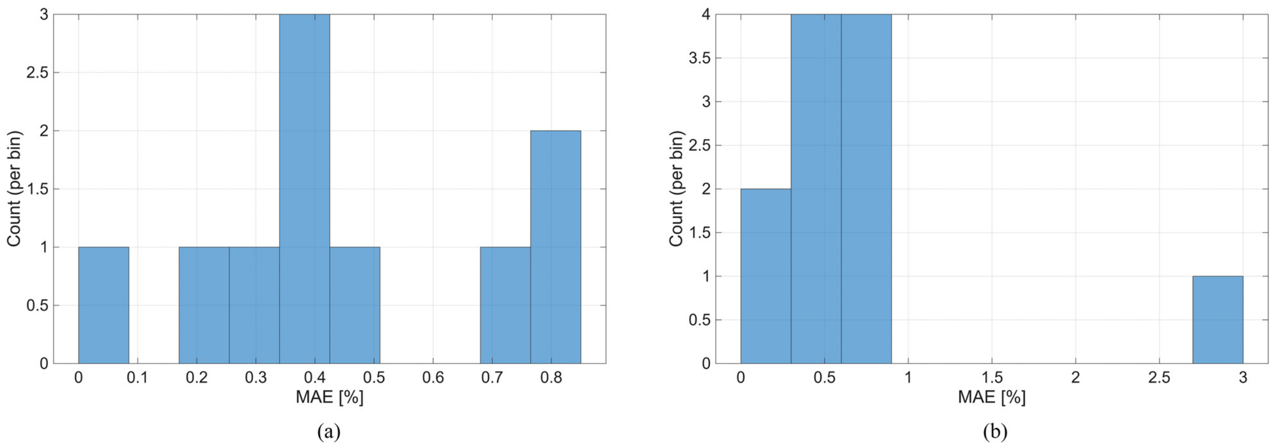

FIG. 9. Distribution of the percentage MAE. Clamped boundary condition, small (a) and large (b) distortion.

depend on two quantities: the acoustic properties of the surrounding medium, through the acoustic wavenumber k_0, and the spatial discretization of the structural domain, through the pairwise distances d_{ij}. The former is adjusted to the prototype operating frequencies with Eq. (7), while the latter is determined from the known prototype geometry. The only requirement is that avatar and prototype share the same grid dimensionality, so that the matrix operations in Eq. (16) remain well defined. A practical choice of implementation is to adopt uniform meshes for both prototype and avatar. Consequently, the pairwise distances between grid points are computed directly from the prototype grid and require no geometric scaling. This avoids conveying geometric distortions from the avatar that would arise if its grid, or its resistance radiation matrix, were used.

Within this theoretical framework, no explicit similitude conditions are required, thus avoiding the limitations associated with their violation. The method is based on general relations, such as the dispersion relation and the phase velocity of flexural waves in thin plates, which depend on the structural operator but are independent of the boundary conditions.

III. WAVENUMBER-BASED METHOD

The wavenumber-based method comprises the following steps, illustrated on the first mode of a simply supported plate.

1. Modal analysis on the avatar, to obtain natural frequencies and mode shapes [Fig. 3(a)].
2. A discrete two-dimensional (2D) spatial Fourier transform of each mode shape, defined on a regular grid, is performed to obtain the corresponding normalized spectrum in wavenumber space [Fig. 3(b) shows the spectrum in the first quadrant]. The wavenumber axes are constructed from the spatial sampling intervals in the x and y directions. A zero-padding factor equal to 25 is adopted in both numerical and experimental validations to increase the sampling density of the discrete wavenumber spectrum.
3. Estimation of the modal wavevector components along the x and y directions. As shown in Sheperd and Hambric (2012) and validated experimentally in Robin *et al.* (2015), these components do not, in general, coincide with the spectral maxima. For a generic rectangular plate, they are given by

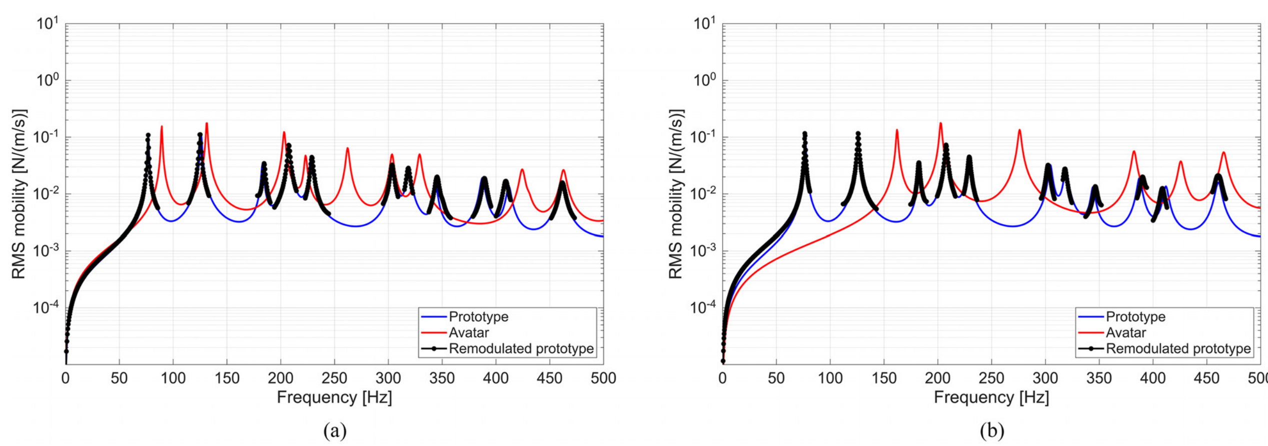

FIG. 10. Reconstruction of the spatially averaged RMS mobility. Clamped boundary condition, small (a) and large (b) distortion.

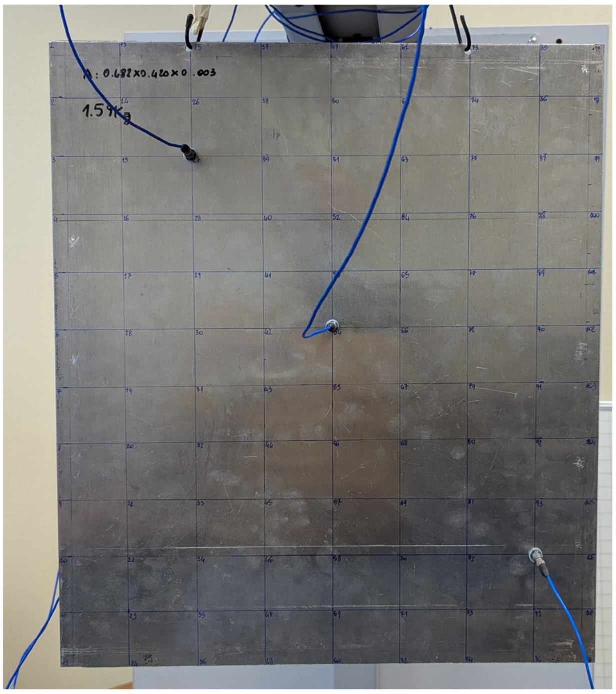

FIG. 11. Experimental setup for the free–free plate.

$$k_{x,mod} = k_{z,x} - \frac{2\pi}{a}, \qquad k_{y,mod} = k_{z,y} - \frac{2\pi}{b}, \tag{17}$$

where $k_{z,x}$ and $k_{z,y}$ denote the wavenumber locations of the first spectral zero after the first peak along the k_x and k_y directions, respectively. For clarity, the estimation procedure is briefly outlined for the x-component. First, the one-dimensional spectral slice along the k_x direction passing through the global maximum of the 2D spectrum is extracted. The first spectral zero following the dominant peak is identified as the first local minimum of the spectral slice, detected at the first sign change of the discrete first-order difference of the spectral amplitude. The modal component $k_{x,mod}$ is subsequently computed using the first relation in Eq. (17). Figure 3(c) illustrates this procedure for the first mode shape: the blue curve represents the extracted spectral slice, the red dashed line indicates $k_{z,x}$ (the first zero after the dominant peak), and the black dashed line corresponds to the estimated modal wavenumber component. The same procedure is applied to determine the y-component.

TABLE III. Geometric and scaling properties of prototype and avatar for the experimental test.

	Prototype	Avatar
a [m]	0.658	0.482
b [m]	0.478	0.420
t [m]	0.003	0.003
r_a	—	1.37
r_b	—	1.14
r_t	—	1.00
r_a/r_b	—	1.20

4. Evaluation of the prototype's modal wavevector components through the scaling laws [Eqs. (9) and (10)].

After step 4, the scale factor of the modal wavevector component can be estimated for each mode, so that Eqs. (7) and (12) are used to reconstruct, mode by mode, the structural response.

IV. NUMERICAL VALIDATION

Numerical validation is performed on two avatars, one with small and one with large distortion, under two boundary conditions: simply supported and clamped. Distortion is measured by the ratio r_a/r_b; as $r_a/r_b \to 1$, the model approaches the complete similitude condition, behaving as a replica.

The plate geometries are reported in Table I and the material properties (aluminum 6061) in Table II.

Before reconstructing the structural response, the estimation of modal wavenumbers via 2D spatial fast Fourier transform (FFT) is verified. For simply supported plates, the modal wavevector components can be written in closed form as (Cremer *et al.*, 2005; Sheperd and Hambric, 2012)

$$k_{x,mod} = \frac{m\pi}{a}, \qquad k_{y,mod} = \frac{n\pi}{b}. \tag{18}$$

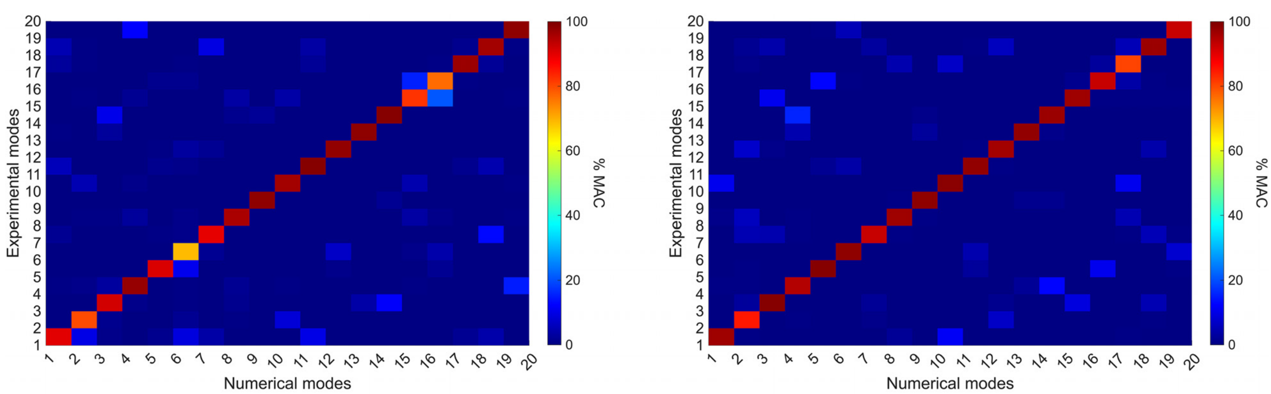

(a) (b)

FIG. 12. MAC between numerical and experimental modes for the prototype (a) and the avatar (b).

https://doi.org/10.1121/10.0042990

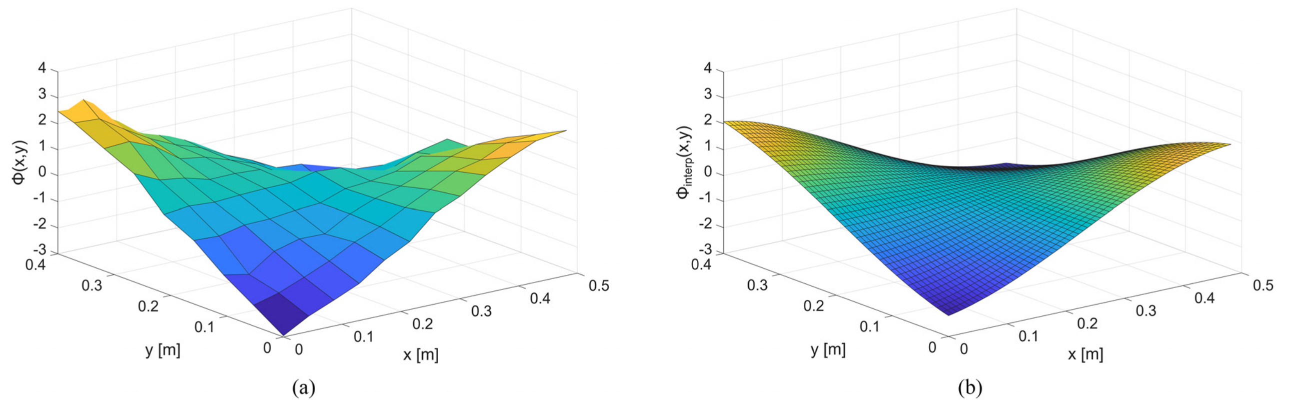

FIG. 13. Experimental mode shape before (a) and after (b) smoothing and interpolation for wavenumber estimation.

Figure 4(a) reports the x components and Fig. 4(b) the y components for the first ten modes: blue markers denote the 2D FFT estimates, red markers the analytical values from Eq. (18). Prototype and small distortion avatar are considered. The two sets overlap, confirming the reliability of the FFT-based estimation.

Results for the response reconstruction are shown in Figs. 5–7 for both avatars. Figure 5 compares ordered natural frequencies within 0–500 Hz for small (a) and large (b) distortion. Blue, red, and black markers represent the natural frequencies of prototype, avatar, and prototype remodulated from those of the avatar. Blue and black markers coincide in both cases, indicating excellent recovery of the prototype natural frequencies.

To quantify the error, Fig. 6 reports histograms of the percentage mean absolute error (MAE), where the vertical axis indicates the number of occurrences within each bin. The maximum values are approximately 0.3% for the small distortion and 0.5% for the large distortion.

Figure 7 shows the spatially averaged RMS mobility over 0–500 Hz. As mentioned, blue, red, and black curves indicate the responses of the prototype, avatar, and prototype reconstructed from the avatar. The reconstruction is performed peak-by-peak: each avatar resonance is remapped in frequency by the mode-dependent frequency scale factor $r_{\omega(m,n)}$ and in amplitude by the mode-dependent velocity scale factor $r_{V(m,n)}$. Agreement is excellent in both frequency and amplitude.

The same analysis under clamped boundary conditions is reported in Figs. 8–10. The reconstruction of the natural frequencies (Fig. 8) exhibits errors below 1% overall (Fig. 9). Compared to the simply supported case, the clamped configuration shows a slightly larger error, with a maximum deviation of 0.8% (versus 0.5% for the small distortion simply supported avatar). The only exception is one high frequency mode exhibiting a MAE of 3% under large distortion. This increase in error is likely related to the different spatial characteristics of clamped mode shapes, which are not purely sinusoidal, leading to less sharply defined peaks in the wavenumber spectrum, and affecting the identification of a dominant modal wavenumber component. Since the angular frequency depends quadratically on the wavenumber, deviations in its estimation are amplified, particularly at higher frequencies. Nevertheless, the overall reconstruction accuracy remains high, and the remodulation of the resonance peaks is successfully achieved (Fig. 10).

These numerical results validate the accuracy and robustness of the proposed method. Experimental tests provide the final validation.

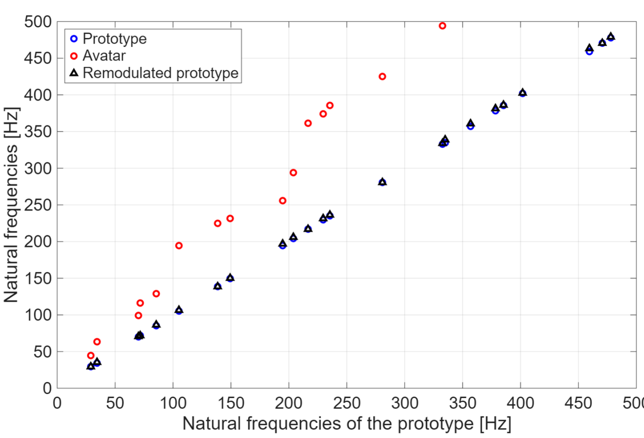

FIG. 14. Reconstruction of prototype natural frequencies from avatar. Free boundary conditions, experimental test.

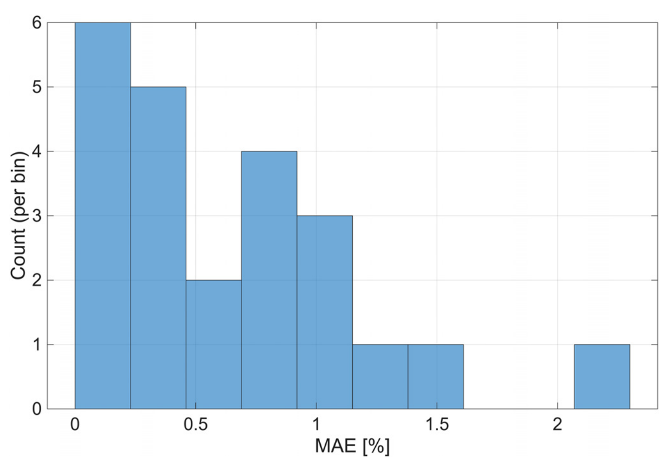

FIG. 15. Distribution of percentage MAE. Free boundary conditions, experimental test.

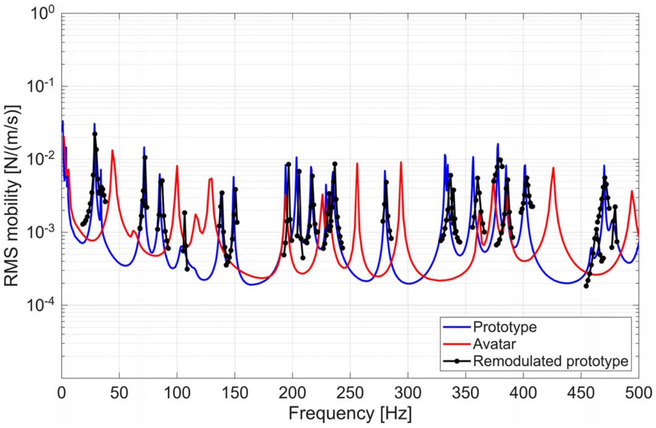

FIG. 16. Reconstruction of the spatially averaged RMS mobility. Free boundary conditions, experimental test.

V. EXPERIMENTAL VALIDATION

Experimental validation is carried out on aluminum plates under free–free boundary conditions. The geometric properties of the prototype and the avatar are summarized in Table III.

Experimental modal analysis is performed using the roving-hammer technique on 108 grid points. Three reference accelerometers are fixed at the non-dimensional coordinates (0.18, 0.25), (0.45, 0.50), and (0.81, 0.88). The suspended plate with sensors is shown in Fig. 11.

The quality of the identified modes is first assessed via the modal assurance criterion (MAC) by comparing the first twenty experimental and numerical modes. The MAC matrices for the prototype and the avatar are reported in Figs. 12(a) and 12(b). The correlation is high across all modes, confirming the reliability of the identified mode shapes.

Since accurate estimation of modal wavenumbers is pivotal for the proposed scaling procedure, the experimental mode shapes are pre-processed before applying the 2D spatial FFT. Figure 13(a) shows a raw experimental mode shape, while Fig. 13(b) shows the same mode after mild spatial smoothing using a Gaussian filter and 2D spline interpolation onto a regular grid, aimed at mitigating measurement noise and obtaining a denser spatial mesh.

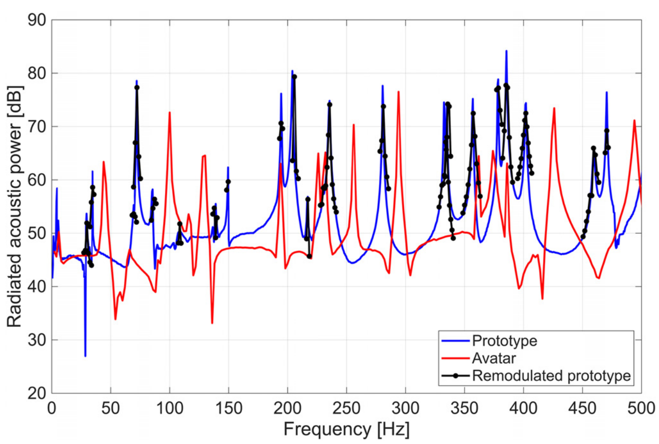

FIG. 17. Reconstruction of the radiated acoustic power (ref. power 1 pW). Free boundary conditions, experimental test.

Figures 14–16 summarize the experimental reconstructions. Figure 14 reports the natural frequencies: the remodulated values show close agreement with those of the prototype across the band, with an overall percentage MAE below 2.5% (Fig. 15). The spatially averaged RMS mobility is reconstructed in Fig. 16; the main resonance peaks are well captured in both frequency and amplitude. Minor mismatches are observed, which are consistent with typical experimental uncertainties and do not affect the overall trends or the peak localization.

Finally, the reconstruction is extended to the radiated acoustic power under mechanical excitation. Radiated acoustic power is not obtained from acoustic measurements but is post-processed from the experimentally measured structural velocity field according to Eqs. (13) and (16). For aluminum plates in air with thickness 0.003 m and material properties reported in Table II, the acoustic and structural wavelengths up to 500 Hz are approximately 0.69 m and 0.24 m, respectively. The adopted patch side lengths for prototype and model range between 0.04 and 0.06 m, corresponding to approximately $\lambda_{str}/6$–$\lambda_{str}/4$ and $\lambda_{ac}/17 - \lambda_{ac}/11$ at 500 Hz. The structural and acoustic fields are, therefore, adequately resolved to satisfy the assumptions underlying Eq. (13) within the considered frequency range. Figure 17 shows that the proposed methodology faithfully reproduces the target spectrum: peak locations and overall spectral shape are preserved. The conversion to decibels and the squared frequency factor in Eq. (16) naturally amplify small amplitude differences, making them more visible, yet these remain within experimental tolerance and do not undermine the accuracy of the reconstruction, widely validated through numerical simulations in Sec. IV.

VI. CONCLUSIONS AND FURTHER RESEARCH

A wavenumber-based approach has been introduced to address the difficulties posed by distorted similitude. The core idea is to exploit mode shape information, through their wavenumber spectra, to reconstruct the structural response mode by mode, bypassing changes in modal ordering that arise under geometric distortions. The formulation does not require explicit similitude conditions and is based on general relations (e.g., the dispersion relation), rather than on boundary condition-specific analytical frequency equations. However, since the method relies on modal similarity, prototype and model must share identical boundary conditions to ensure comparability of the mode shapes. Explicit knowledge of the boundary condition type is not required, provided that both configurations are subject to the same boundary constraints.

Numerical and experimental studies on multiple avatars and boundary conditions indicate that the method reliably reconstructs natural frequencies, mobility FRFs, and radiated acoustic power. As such, it provides a consistent reconstruction of vibroacoustic characteristics, from natural frequencies to derived metrics that depend on post-processed response data.

Some limitations remain. The scaling relies on structure-dependent dispersion parameters (for example, the bending wave speed in thin plates) and assumes mode-shape correspondence between prototype and avatar, i.e., topologically similar modes. Significant changes in boundary conditions or geometry (like plates versus cylindrical shells), as well as configurations where distortions alter the lay-up of laminated plates, may violate this assumption and are currently outside the method's scope.

With this in mind, the proposed method provides both a solid basis and a novel framework for the structural similitude field. Accordingly, future applications should address more complex structures, such as stiffened plates or cylinders, and structural configurations, such as sandwich structures, with the twofold aim of extending its applicability and tackling its main issues.

AUTHOR DECLARATIONS

Conflict of Interest

The author has no conflicts to disclose.

DATA AVAILABILITY

The data that support the findings of this study are available from the corresponding author upon reasonable request.

Adams, C., Bös, J., Slomski, E. M., and Melz, T. (**2018**). "Scaling laws obtained from a sensitivity analysis and applied to thin vibrating structures," Mech. Syst. Sig. Process. **110**, 590–610.

Berry, A., Robin, O., Franco, F., De Rosa, S., and Petrone, G. (**2020**). "Similitude laws for the sound radiation of flat orthotropic flexural panels," J. Sound Vib. **489**, 115636.

Casaburo, A., Petrone, G., Franco, F., and De Rosa, S. (**2019**). "A review of similitude methods in structural engineering," Appl. Mech. Rev. **71**(3), 030802.

Casaburo, A., Petrone, G., Meruane, V., Franco, F., and De Rosa, S. (**2021**). "The vibroacoustic behaviour of aluminium foam sandwich panels in similitude," J. Sandwich Struct. Mater. **23**(8), 4170–4195.

Cremer, L., Heckl, M., and Petersson, B. A. T. (**2005**). *Structure-Borne Sound. Structural Vibrations and Sound Radiation at Audio Frequencies*, 3rd ed. (Springer Berlin, Heidelberg).

Davey, K., Darvizeh, R., Golbaf, A., and Sadeghi, H. (**2020**). "The breaking of geometric similarity," Int. J. Mech. Sci. **187**, 105925.

De Rosa, S., and Franco, F. (**2008**). "Exact and numerical responses of a plate under a turbulent boundary layer excitation," J. Fluids Struct. **24**(2), 212–230.

De Rosa, S., Franco, F., Petrone, G., Casaburo, A., and Marulo, F. (**2021**). "A versatile offset operator for the discrete observation of objects," J. Sound Vib. **500**, 116019.

Elliott, S. J., and Johnson, M. E. (**1993**). "Radiation modes and the active control of sound power," J. Acoust. Soc. Am. **94**, 2194–2204.

Franco, F., Berry, A., Petrone, G., De Rosa, S., Ciappi, E., and Robin, O. (**2020**). "Structural response of stiffened plates in similitude under turbulent boundary layer excitation," J. Fluids Struct. **98**, 103119.

Franco, F., Robin, O., Ciappi, E., De Rosa, S., Berry, O., and Petrone, G. (**2019**). "Similitude laws for the structural response of flat plates under a turbulent boundary layer excitation," Mech. Syst. Sig. Process. **129**, 590–613.

Goodier, J. N., and Thomson, W. T. (**1944**). "Applicability of similarity principles to structural models," Technical Report NACA-TN-933 (NACA, Washington, DC).

Hambric, S., and Barnard, A. R. (**2018**). "Tutorial on wavenumber transforms of structural vibration fields," in *Proceedings of the 47th International Congress and Exposition on Noise Control Engineering*, Chicago, IL.

Kasivitamnuay, J., and Singhatanadgid, P. (**2005**). "Application of an energy theorem to derive a scaling law for structural behaviors," Int. J. Sci. Technol. Thammasat **10**(4), 33–40.

Leissa, A. W. (**1969**). "Vibration of plates," Technical Report NASA-SP-160 (NASA, Washington, DC).

Luo, Z., Wang, Y., Zhu, Y., and Wang, D. (**2016**). "The dynamic similitude design method of thin walled structures and experimental validation," Shock Vib. **2016**, 6836183.

Meruane, V., De Rosa, S., and Franco, F. (**2016**). "Numerical and experimental results for the frequency response of plates in similitude," Proc. Inst. Mech. Eng., Part C: J. Mech. Eng. Sci. **230**(18), 3212–3221.

Plouseau-Guédé, X., Berry, A., Maxit, L., and Meyer, V. (**2025**). "Similitude laws for the vibroacoustic response of fluid-loaded plates under a turbulent boundary layer excitation," J. Acoust. Soc. Am. **157**, 595–605.

Rezaeepazhand, J., and Yazdi, A. A. (**2011**). "Similitude requirements and scaling laws for flutter prediction of angle-ply composite plates," Composites Part B **42**(1), 51–56.

Robin, O., Berry, A., Atalla, N., Hambric, S. A., and Shepherd, M. R. (**2015**). "Experimental evidence of modal wavenumber relation to zeros in the wavenumber spectrum of a simply supported plate," J. Acoust. Soc. Am. **137**(5), 2978–2981.

Sheperd, M. R., and Hambric, S. A. (**2012**). "Comment on plate modal wavenumber transforms in Sound and Structural Vibration [Academic Press (**1987**, 2007)]," J. Acoust. Soc. Am. **132**(4), 2155–2157.

Simitses, G. J., and Rezaeepazhand, J. (**1993**). "Structural similitude for laminated structures," Compos. Eng. **3**(7–8), 751–765.

Yazdi, A. A., and Rezaeepazhand, J. (**2011**). "Accuracy of scale models for flutter prediction of cross-ply laminated plates," J. Reinf. Plast. Compos. **30**(1), 45–52.